

# Hybrid Analytical Modeling: Fourier Modeling Combined with Mesh-Based Magnetic Equivalent Circuits

K.J.W. Pluk, J.W. Jansen, and E.A. Lomonova

Department of Electrical Engineering, Eindhoven University of Technology, Eindhoven, The Netherlands

This paper presents a hybrid analytical modeling method which integrates a mesh-based magnetic equivalent circuit model with the Fourier modeling approach. This hybrid analytical modeling is capable of correctly predicting the electromagnetic field distributions for various two-dimensional geometries. The generalized approach of the presented hybrid modeling concept, makes the modeling technique applicable to a wide range of electromagnetic devices. By only meshing the parts of the domain in the vicinity of the high permeable materials, the increase in computational effort is limited compared to the sole use of Fourier modeling. The proposed hybrid analytical modeling method predicts the force in the geometry with  $\geq 97$  [%] accuracy with respect to finite element analysis.

**Index Terms**—Analytical models, electromagnetic modeling, Fourier analysis, magnetic equivalent circuit, reluctance network

## LIST OF SYMBOLS

$\vec{A}$	Magnetic vector potential	[Wb m <sup>-1</sup> ]
$\vec{B}$	Magnetic flux density vector	[T]
$\vec{H}$	Magnetic field strength vector	[A m <sup>-1</sup> ]
$\vec{J}$	Current density	[A m <sup>-2</sup> ]
$\vec{M}_0$	Magnetization vector	[A m <sup>-1</sup> ]
$\hat{e}$	Unit vector	[—]
$B_r$	Remanent flux density	[T]
$\mu_0$	Permeability of vacuum $4\pi \cdot 10^{-7}$	[H m <sup>-1</sup> ]
$\mu_r$	Relative permeability	[—]
$i$	Arbitrary Fourier region	[—]
$m$	Arbitrary MEC-region	[—]
$k$	Arbitrary MEC-element number	[—]
$\psi$	Magnetic scalar potential	[A]
$\varphi$	Magnetic flux	[Wb]
$\omega_n^i$	Spatial frequency	[m <sup>-1</sup> ]
$n$	Harmonic number	[—]
$N$	Total number of harmonics	[—]
$x_p$	Width of the periodicity	[m]

## I. INTRODUCTION

**E**LECTROMAGNETIC field modeling is a crucial step in the design process of electromagnetic devices. Very extensive magnetic field modeling is necessary to achieve an optimal design. A lot of research and development is conducted in methods to predict the magnetic field distribution inside electromagnetic structures. Especially during the design of an electromagnetic device, the computational efforts should be low to enable a broad exploratory investigation of the design space. Therefore, the numerical methods (such as Finite Element Analysis [1]) are less convenient, and if possible the reduction from a three-dimensional (3-D) geometry to a two-dimensional (2-D) model is made.

Analytical or semi-analytical modeling methods are less time consuming than the numerical methods, however, usually the accuracy that can be obtained with these methods is lower. During the design, the accuracy of the magnetic field calculations is less important which makes the (semi-)analytical modeling methods a suitable way to predict the magnetic field. In the literature, many (semi-)analytical methods are discussed, including

- Magnetic Equivalent Circuit (MEC) modeling [2, 3];
- (surface) charge modeling (CM) [4–7];
- Fourier modeling [8–11].

For applications where the flux paths are largely pre-defined by the high-permeable materials, the MEC modeling is usually the appropriate choice. This pre-defined path enables the usage of flux-tubes to simplify the geometry, and therewith, enables the calculation the magnetic field. To apply the MEC modeling to more complex geometries, the modeling can be extended with the Tooth Contour Method [12] or a conformal mapping technique [13]. The extension enables the calculation of the non-arbitrary couplings between, for instance, the stator and the rotor.

For unbounded problems where no coils and no high-permeable material is present, the surface charge modeling is one of the preferable options. The surface charge modeling is extended by applying images [14, 15] or by including the secondary magnetic field [16] to mimic the high-permeable materials in the vicinity.

Geometries with repeating geometrical patterns are a typical example for a spatial harmonic description such as Fourier modeling. Using the Fourier modeling, the different materials are incorporated as regions, where in each region a Fourier based expression for the magnetic field is used. However, this definition is limited to regions, and therefore materials, of equal width (in the periodic direction). Extending the Fourier modeling with mode-matching, regions (i.e. material

Corresponding author: K.J.W. Pluk (e-mail: K.J.W.Pluk@tue.nl)

blocks) with a different width can be incorporated [9, 17]. Unfortunately, an additional physically non-existing boundary is necessary to obtain a solution. Furthermore, in situations where small features are important, the number of harmonics can be limited due to the high fundamental spatial frequency, while a large number of harmonics is required to achieve sufficient accuracy.

This paper proposes a semi-analytical modeling method capable of incorporating high permeable materials with small features (such as saliency, tooth tips, slot shapes and small slots), while the presence of both coils and magnets is possible. The hybrid analytical modeling method discussed in this paper combines Fourier modeling with a mesh-based magnetic equivalent circuit model. The Fourier modeling is extensively discussed by Gysen [9], while the mesh-based MEC modeling is known from [18–20]. The combination of a mesh-based MEC modeling with harmonic modeling methods is proposed in [21–24]. Where Ouagued [21], Barakat [22] and Laoubi [23] only connect the mesh-based modeling to the harmonic modeling on one side, this paper applies a bi-directional coupling on both sides of the MEC-region.

In this paper, the hybrid analytical modeling method is described in a generalized manner for two-dimensional Cartesian situations. First, the focus is on the model formulation before introducing the full modeling methodology and the boundary conditions. Afterwards a validation of the modeling method is performed using a comparison with 2-D finite element models for two different geometries.

## II. MODEL FORMULATION

### A. Model Assumptions

To apply the hybrid modeling to a certain situation or geometry, the following assumptions are made:

- 1) the problem is formulated in 2-D
- 2) the problem is time independent (i.e. quasi-static)
- 3) periodicity is present in the  $x$ -direction
- 4) only homogeneous, isotropic, linear materials are used
- 5) magnetic field sources (magnets and coils) are homogeneous and invariant in the  $z$ -direction.

To enable a Fourier based description of the magnetic field, periodicity is implied, where in this model the periodic direction is chosen along the  $x$ -direction. If no actual periodicity is present, the periodicity should be chosen such that the influence of the adjacent periods on the observed geometry is limited. Choosing a very large period seems ideal for these cases, however, this will directly result in a large number of harmonics required, and therefore, a large computational price.

The semi-analytical modeling given in this paper is only valid under the assumption that all materials used are homogeneous, isotropic and linear. In the initial design of an electromagnetic device, it is sufficient to know the value of the magnetic flux density inside the materials to indicate whether the material might saturate, therefore, the assumed linearity of the materials is not an issue. The influence of the possible non-homogeneity and anisotropy of the materials is marginal and, therefore, negligible.

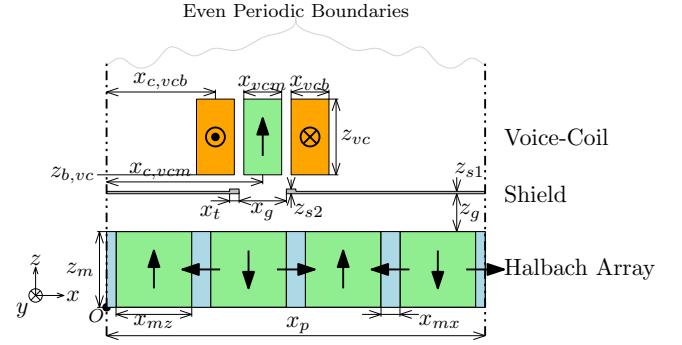


Fig. 1. Shielding geometry, a locally thickened magnetic shield with a hole between a permanent magnet Halbach array and voice-coil actuator.

The magnetic field sources, i.e. permanent magnets and coils, should be homogeneous in their amplitude and no variations in the  $z$ -direction are allowed. The invariance in the  $z$ -direction in the modeling is ensured by a proper division of the geometry in regions, while the homogeneity of the sources is a necessity for the source description in the model. Non-homogeneity of a source in the  $x$ -direction can be incorporated by placing multiple sources with different amplitudes adjacent to each other, i.e. a discrete description of variation in the source. Furthermore, the permanent magnets in the problem are magnetized in the  $x$  or the  $z$ -direction, while only current sources in the  $y$ -direction are included, due to the assumed 2-D description.

### B. Electromagnetic examples

The proposed hybrid analytical modeling method is applied on two electromagnetic examples, one concerning shielding, and one showing the capabilities of the modeling method in motor design.

The geometry shown in Fig. 1 consists of a permanent magnet Halbach array, above which a voice coil actuator, with a permanent magnet, is located. The permanent magnet of the voice coil actuator experiences an undesired force caused by the electromagnetic fields originating from the Halbach array. To reduce the magnetic field of the permanent magnet array, a magnetic shielding plate is introduced between the permanent magnet array and the voice coil actuator. Since a solid ferromagnetic shield would give a large reluctance force on the permanent magnet of the voice coil actuator, a hole in the magnetic shield is located, directly underneath the permanent magnet. Around the hole, the magnetic shield, is locally thickened. The dimensions and material parameters for the shielding geometry are given in Table I.

To show the possibilities of the modeling method for the machine design, a multi-tooth flux-switching permanent magnet linear motor, with double saliency, is modeled. Due to the capability of the proposed modeling method to include small features with a high-permeability, the hybrid analytical modeling method is suited for analyzing design features such as tooth tips, slot shapes and saliency. The chosen multi-tooth flux-switching permanent magnet linear motor geometry and its dimensions are based on the motor presented in [25].

TABLE I  
GEOMETRICAL AND MATERIAL PARAMETERS FOR SHIELDING GEOMETRY

Parameter	Value	Description
$x_p$	100 [mm]	Width of the periodicity
$x_{mz}$	20 [mm]	Width of magnets in $z$ -direction
$x_{mx}$	5 [mm]	Width of magnets in $x$ -direction
$x_g$	14 [mm]	Width of the hole in the shield
$x_t$	4 [mm]	Width of the thickening of the shield
$x_{vcm}$	10 [mm]	Width of the voice coil magnet
$x_{vcb}$	10 [mm]	Width of the voice coil bundle
$x_{c,vcb}$	29 [mm]	Center of the voice coil bundle
$x_{c,vcm}$	43 [mm]	Center of the voice coil magnet
$z_m$	20 [mm]	Height of the magnets
$z_{g1}$	10 [mm]	Gap between magnets and shield
$z_{s1}$	1 [mm]	Thickness of the shield
$z_{s2}$	2 [mm]	Thickness of the shield with thickening
$z_{vc}$	20 [mm]	Height of the voice coil
$z_{b,vc}$	35 [mm]	Bottom coordinate of the voice coil
$B_r$	1.4 [T]	Remanence of the permanent magnets
$J$	5 [A/mm <sup>2</sup> ]	Current density in voice coil
$\mu_{r,m}$	1.05 [-]	Relative permeability of magnets
$\mu_{r,s}$	1500 [-]	Relative permeability of the shield

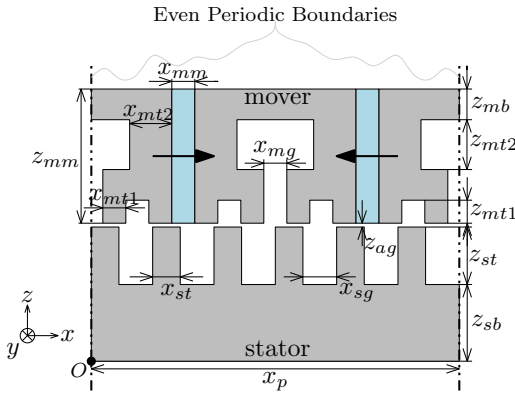


Fig. 2. A multi-tooth flux-switching permanent magnet linear motor geometry.

The geometry is shown in Fig. 2, while the geometrical and material parameters are specified in Table II.

### C. Division in Regions

Observing the geometries shown in Fig. 1 and 2, the coordinate system is defined such that the present periodicity is aligned with the  $x$ -axis and the invariant direction is chosen in the  $y$ -direction. The  $z$ -direction is the direction with the changing materials. For the hybrid analytical modeling, the geometry should be divided in regions where each region contains only one material, and has a width equal to the periodicity. The regions are numbered ascending in the  $z$ -direction.

A permanent magnet is incorporated in the modeling as a region containing the magnetic material while the permanent magnet is represented by a block-shaped magnetization function. Equivalently, the coil bundles are modeled by a region with  $\mu_r = 1$  [-] and a block-shaped current density function (see Region 6 in Fig. 3).

In general, in the hybrid analytical modeling all high-permeable materials ( $\mu_r \gg 10$ ) that do not have a width equal to the periodicity, are modeled using a MEC-region.

TABLE II  
GEOMETRICAL AND MATERIAL PARAMETERS FOR MULTI-TOOTH MOTOR GEOMETRY

Parameter	Value	Description
$x_p$	48 [mm]	Width of the periodicity
$x_{st}$	3.6 [mm]	Width stator teeth
$x_{sg}$	4.4 [mm]	Width of gap between stator teeth
$x_{mt1}$	3 [mm]	Width of small mover teeth
$x_{mg}$	3 [mm]	Width of gap between small mover teeth
$x_{mm}$	3 [mm]	Width of mover magnets
$x_{mt2}$	5.5 [mm]	Width of large mover teeth
$z_{sb}$	10 [mm]	Height of stator backiron
$z_{st}$	7.5 [mm]	Height of stator teeth
$z_{ag}$	0.5 [mm]	Height of airgap
$z_{mt1}$	3 [mm]	Height of small mover teeth
$z_{mt2}$	6.5 [mm]	Height of large mover teeth
$z_{mb}$	4 [mm]	Height of mover backiron
$z_{mm}$	17.5 [mm]	Height of mover magnet
$B_r$	1.2 [T]	Remanence of the permanent magnets
$\mu_{r,m}$	1 [-]	Relative permeability of magnets
$\mu_{r,i}$	750 [-]	Relative permeability of the iron

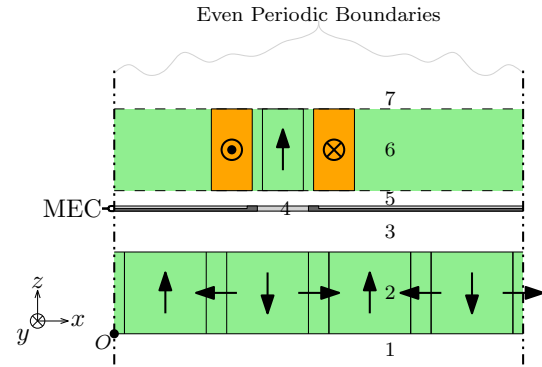


Fig. 3. The division in regions for the shielding geometry shown in Fig. 1.

Inside this MEC-region all materials (high-permeable, but also air) and sources are meshed. Therefore, in the geometry of Fig. 1 the magnetic shield with its thickened parts are modeled using the mesh-based magnetic equivalent circuit modeling.

For the geometry in Fig. 2, the stator teeth are modeled as a MEC-region, while the full mover is modeled as another MEC-region. The obtained MEC-regions have a width equal to the periodicity, while the mesh inside the MEC-regions is chosen such that the material changes are incorporated.

The resulting division in regions for the shielding geometry is given in Fig. 3 where Region 4 is the MEC-region. For the multi-tooth motor, Regions 3 and 5 are MEC-regions as shown in Fig. 4, where the division in regions is shown. Throughout most of this manuscript a general definition of the regions is used, where  $i$  is an arbitrary Fourier region, while  $m$  is used for the MEC-region.

### D. Definition of MEC-element

As previously indicated, inside the MEC-region a mesh-based discretization is used. The MEC-region is meshed in the  $x, z$ -plane with rectangular elements. Even though the meshing in both the  $x$ - and the  $z$ -direction can be non-uniform, in the used formulation, all elements in the  $z$ -direction with a certain

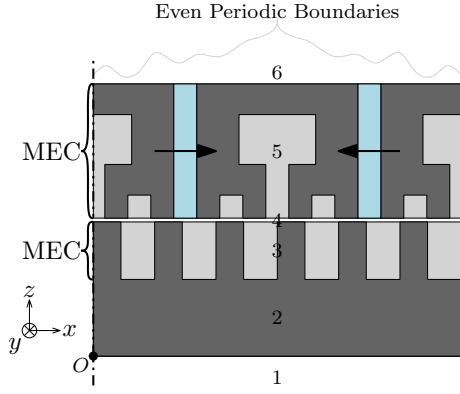


Fig. 4. The division in regions for the multi-tooth flux-switching permanent magnet linear motor of Fig. 2.

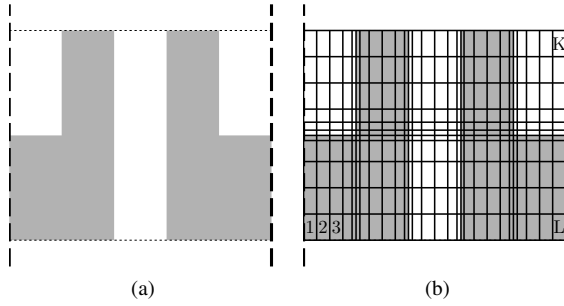


Fig. 5. The meshing principle illustrated on a simplified system where (a) shows the geometry and (b) the obtained meshing including numbering and locally increased mesh-density. (The dashed (vertical) lines indicate the periodic boundaries.)

$x$ -coordinate will have an equal width in the  $x$ -direction and vice-versa. The meshing of the MEC-region is performed such that the material boundaries of the geometry are coinciding with the edges of the MEC-elements. The number of MEC-elements inside the MEC-region can be increased for a more accurate solution. Due to the possibility of a non-uniform mesh size, local increase of mesh-density is possible. However, in the used formulation a local increase of the mesh in the  $x$ -direction will be visible throughout the full  $z$ -direction of the MEC-region as is shown in Fig. 5 (where the numbering of the mesh-elements is indicated as well).

With the described meshing method, the resulting MEC-elements will contain only one material (i.e. iron, air of magnet). In each MEC-element, a potential node is defined in its geometrical center. From this potential node towards all four sides of the MEC-element a magnetic reluctance is present. In both the positive and negative  $x$ -direction, a reluctance is assumed, which covers half of the width of the MEC-element. While the reluctances in the positive and negative  $z$ -direction each cover half of the height of the MEC-element. The reluctances used are calculated according to

$$\mathcal{R}_{x+}^k = \mathcal{R}_{x-}^k = \frac{l_x^k}{2\mu_0\mu_r^k S_{yz}^k} \quad (1)$$

$$\mathcal{R}_{z+}^k = \mathcal{R}_{z-}^k = \frac{l_z^k}{2\mu_0\mu_r^k S_{xy}^k} \quad (2)$$

where  $l_x^k$  and  $l_z^k$  are the sizes of MEC-element  $k$  in the  $x$ -

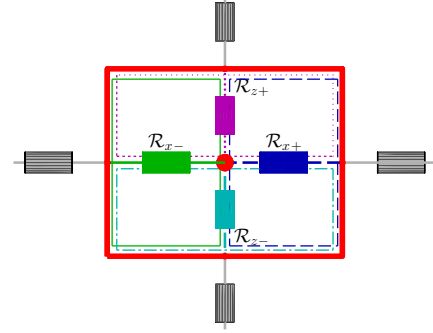


Fig. 6. Illustration of a mesh element in the mesh-based MEC modeling. The thick red solid-line square indicates the actual MEC-element. Centered in the element, the red circular marker, indicates the potential node. The reluctance elements are indicated by the  $\mathcal{R}_{x+}$ ,  $\mathcal{R}_{x-}$ ,  $\mathcal{R}_{z+}$  and  $\mathcal{R}_{z-}$ .

and  $z$ -direction, respectively, where  $\mu_0 = 4\pi \cdot 10^{-7}$  [H/m] is the permeability of vacuum,  $\mu_r^k$  is the relative permeability of the material in this MEC-element. Furthermore,  $S_{xy}^k$  and  $S_{yz}^k$  are the cross-sectional areas of MEC-element  $k$  in the  $x, y$ - and  $y, z$ -plane, respectively. Due to the assumption of a 2-D geometry, a unity size of a MEC-element in the  $y$ -direction is chosen.

The reluctances in each MEC-element are illustrated in Fig. 6, where the thick (red) solid-line rectangle indicates the actual mesh element, and the red point gives the potential node. Furthermore, the solid, dashed, dotted and dash-dotted lines illustrate the flux-tubes corresponding with the reluctance elements.

With the reluctances, the center node is coupled to the adjacent MEC-elements on the top, bottom, left and right, to complete the MEC-region. The periodicity inside the MEC-region is taken into account by assuming that the last element in the  $x$ -direction is adjacent to the first element in the  $x$ -direction and vice-versa.

### III. MODELING METHODOLOGY

#### A. Fourier Modeling Description

In order to solve the magnetostatic field distribution in a region, the magnetic flux density,  $\vec{B}$ , can be written in terms of the magnetic vector potential,  $\vec{A}$  as explained in [9]. By assuming a 2-D geometry with the invariancy in the  $y$ -direction, where the magnetization is only possible in the  $x$ - and  $z$ -direction and is independent of  $z$ , and where only a current density in the  $y$ -direction exists, a second-order differential equation is obtained as given by

$$\nabla^2 A_y(x, z) = -\mu_0\mu_r J_y(x) + \mu_0 \frac{\partial M_z(x)}{\partial x} \quad (3)$$

where  $\mu_r$  is the relative permeability of the material in the region,  $J_y$  is the current density in the  $y$ -direction and  $M_z$  is the residual magnetization in the  $z$ -direction.

In each region the solution for  $A_y^i$ , where  $i$  is an arbitrary region with a Fourier description, is chosen such that the Poisson equation (3) is fulfilled, while concerning the periodicity

in the  $x$ -direction. The chosen general solution for  $A_y$  is given by

$$A_y^i(x, z) = A_{y0}^i(z) + \sum_{n=1}^N [A_{ycn}^i(z) \cos(\omega_n^i x) + A_{ysn}^i(z) \sin(\omega_n^i x)] \quad (4)$$

where  $N$  is the total number of harmonics taken into account, and where  $A_{y0}^i(z)$ ,  $A_{ycn}^i(z)$  and  $A_{ysn}^i(z)$  are given by

$$A_{y0}^i(z) = -\mu_0 M_{x0}^i z \quad (5)$$

$$A_{ycn}^i(z) = -\frac{1}{\omega_n^i} q_n^i e^{\omega_n^i z} - \frac{1}{\omega_n^i} r_n^i e^{-\omega_n^i z} - \frac{\mu_0}{\omega_n^i} M_{zsn}^i - \frac{\mu_0 \mu_r}{(\omega_n^i)^2} J_{ycn}^i \quad (6)$$

$$A_{ysn}^i(z) = -\frac{1}{\omega_n^i} s_n^i e^{\omega_n^i z} - \frac{1}{\omega_n^i} t_n^i e^{-\omega_n^i z} + \frac{\mu_0}{\omega_n^i} M_{zcn}^i - \frac{\mu_0 \mu_r}{(\omega_n^i)^2} J_{ysn}^i \quad (7)$$

where  $q_n^i$ ,  $r_n^i$ ,  $s_n^i$  and  $t_n^i$  are the a-priori unknown coefficients which have to be solved using boundary conditions, and where  $M_{zsn}^i$ ,  $M_{zcn}^i$ ,  $J_{ysn}^i$  and  $J_{ycn}^i$  are the sine and cosine terms of the Fourier description of the magnetization in the  $z$ -direction and the current density in the  $y$ -direction, respectively. Furthermore,  $M_{x0}^i$  is the DC-term in the magnetization in the  $x$ -direction which will occur in the boundary description of the tangential magnetic field strength (later on), and  $\omega_n^i$  is  $n$  times the fundamental spatial frequency  $\omega_0$  which is determined from the periodicity according to

$$\omega_n^i = n\omega_0 = n \frac{2\pi}{x_p} \quad (8)$$

where  $x_p$  is the width of the periodicity.

With the given definition of the magnetic vector potential, the magnetic flux density description can be derived according to

$$\vec{B}^i(x, z) = -\frac{\partial A_y^i(x, z)}{\partial z} \hat{e}_x + \frac{\partial A_x^i(x, z)}{\partial x} \hat{e}_z. \quad (9)$$

The magnetic flux density inside an arbitrary Fourier region is given by

$$\vec{B}^i(x, z) = B_x^i(x, z) \hat{e}_x + B_z^i(x, z) \hat{e}_z \quad (10)$$

$$B_x^i(x, z) = \mu_0 M_{x0}^i + \sum_{n=1}^N [B_{xsn}^i(z) \sin(\omega_n^i x) + B_{xcn}^i(z) \cos(\omega_n^i x)] \quad (11)$$

$$B_z^i(x, z) = \sum_{n=1}^N [B_{zsn}^i(z) \sin(\omega_n^i x) + B_{zcn}^i(z) \cos(\omega_n^i x)] \quad (12)$$

where  $B_{xsn}^i$ ,  $B_{xcn}^i$ ,  $B_{zsn}^i$  and  $B_{zcn}^i$  are given by

$$B_{xsn}^i(z) = s_n^i e^{\omega_n^i z} - t_n^i e^{-\omega_n^i z} \quad (13)$$

$$B_{xcn}^i(z) = q_n^i e^{\omega_n^i z} - r_n^i e^{-\omega_n^i z} \quad (14)$$

$$B_{zsn}^i(z) = q_n^i e^{\omega_n^i z} + r_n^i e^{-\omega_n^i z} + \mu_0 M_{zsn}^i + \frac{\mu_0 \mu_r}{\omega_n^i} J_{ycn}^i \quad (15)$$

$$B_{zcn}^i(z) = -s_n^i e^{\omega_n^i z} - t_n^i e^{-\omega_n^i z} + \mu_0 M_{zcn}^i - \frac{\mu_0 \mu_r}{\omega_n^i} J_{ysn}^i. \quad (16)$$

## B. Source Term Description

In the magnetic flux density description, the magnetization and current density terms are derived as a Fourier description. In general, a permanent magnet will be replaced by a rectangular shaped magnetization function. Equivalently, a rectangular shaped current density function is assumed. These magnetization and current density functions are described as

$$M_x^i(x) = M_{x0}^i + \sum_{n=1}^N [M_{xsn}^i \sin(\omega_n^i x) + M_{xcn}^i \cos(\omega_n^i x)] \quad (17)$$

$$M_z^i(x) = M_{z0}^i + \sum_{n=1}^N [M_{zsn}^i \sin(\omega_n^i x) + M_{zcn}^i \cos(\omega_n^i x)] \quad (18)$$

$$J_y^i(x) = J_{y0}^i + \sum_{n=1}^N [J_{ysn}^i \sin(\omega_n^i x) + J_{ycn}^i \cos(\omega_n^i x)]. \quad (19)$$

Except for  $M_{x0}$ , all DC-terms can be neglected since only  $M_{x0}$  is required in the Fourier description. The sine and cosine terms of the magnetization in the  $x$ -direction are not directly visible in the magnetic flux density description, however these terms are used in the boundary conditions.

According to the general Fourier theory [9], the source terms (i.e.  $M_{x0}$ ,  $M_{xsn}$ ,  $M_{xcn}$ ,  $M_{z0}$ ,  $M_{zsn}$ ,  $M_{zcn}$ ,  $J_{y0}$ ,  $J_{ysn}$  and  $J_{ycn}$ ), when considering the rectangular shaped definition of the source curves, are given by

$$M_{x0}^i = \frac{1}{x_p} \sum_{s_x^i=1}^{S_x^i} \hat{M}_{x^i}^{s_x^i} (x_1^{s_x^i} - x_0^{s_x^i}) \quad (20)$$

$$M_{xsn}^i = \frac{2}{x_p} \sum_{s_x^i=1}^{S_x^i} \frac{\hat{M}_{x^i}^{s_x^i}}{\omega_n^i} \left( \cos(\omega_n^i x_0^{s_x^i}) - \cos(\omega_n^i x_1^{s_x^i}) \right) \quad (21)$$

$$M_{xcn}^i = \frac{2}{x_p} \sum_{s_x^i=1}^{S_x^i} \frac{\hat{M}_{x^i}^{s_x^i}}{\omega_n^i} \left( \sin(\omega_n^i x_1^{s_x^i}) - \sin(\omega_n^i x_0^{s_x^i}) \right) \quad (22)$$

where  $s_x^i$  is a counter through the magnets magnetized in the  $x$ -direction in region  $i$ , and  $x_0$  and  $x_1$  are the  $x$ -coordinate of the left and right sides of the magnet, respectively, and where  $\hat{M}_{x^i}^{s_x^i}$  is the amplitude of the magnetization of this magnet. Equivalently, the source terms for  $M_z$  and  $J_y$  are found.

A permanent magnet for which the magnetization is not aligned with either the  $x$ - or  $z$ -direction, is modeled by

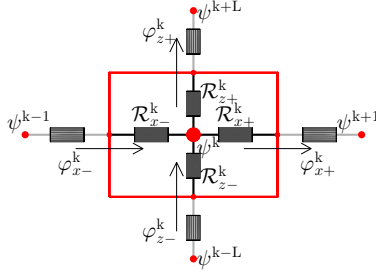


Fig. 7. Illustration of the magnetic flux,  $\phi$ , reluctance,  $\mathcal{R}$ , and magnetic potential,  $\psi$ , involved in the magnetic equivalent of Kirchhoff's current law (23).

superimposing a magnet magnetized in  $x$ -, and a magnet magnetized in the  $z$ -direction. The strength of these magnets is obtained by using the vector projection on the axis of the original magnetization.

### C. MEC Modeling Description

The harmonic modeling method described above is limited to describing situations where the high permeable material spans the full period of the model. The inclusion of small high-permeable features (such as tooth-tips, slot shapes and small slots) is not directly possible. Therefore, the mesh-based Magnetic Equivalent Circuit (MEC) modeling technique is applied to model the high permeable features that are smaller than the period of the Fourier model.

As previously indicated, inside each MEC-element a potential-node is defined. With the magnetic equivalence of Kirchhoff's current law, the magnetic scalar potential distribution in the center nodes of the MEC-elements in the MEC-region is found. The magnetic equivalence of Kirchhoff's current law applied to MEC-element  $k$  (shown in Fig. 7) gives

$$\sum \varphi_{in} = \sum \varphi_{out} \Rightarrow \varphi_{x-} + \varphi_{z-} - \varphi_{x+} - \varphi_{z+} = 0 \quad (23)$$

where  $\varphi$  is the magnetic flux in a branch, calculated according to

$$\varphi_{x-}^k = \frac{\psi^{k-1} - \psi^k}{\mathcal{R}_{x+}^{k-1} + \mathcal{R}_{x-}^k} \quad (24)$$

$$\varphi_{x+}^k = \frac{\psi^k - \psi^{k+1}}{\mathcal{R}_{x-}^{k+1} + \mathcal{R}_{x+}^k} \quad (25)$$

$$\varphi_{z-}^k = \frac{\psi^{k-L} - \psi^k}{\mathcal{R}_{z+}^{k-L} + \mathcal{R}_{z-}^k} \quad (26)$$

$$\varphi_{z+}^k = \frac{\psi^k - \psi^{k+L}}{\mathcal{R}_{z-}^{k+L} + \mathcal{R}_{z+}^k} \quad (27)$$

where  $\psi^k$  is the magnetic scalar potential at the center node of MEC-element  $k$ , and where  $L$  is the number of MEC-elements in a layer of the MEC-region (i.e. all elements in the MEC-region with an equal  $z$ -coordinate). Therefore, MEC-element  $k+L$  is directly on top of element  $k$ .

To include the periodicity in the MEC-layer, for the far left and far right MEC-elements, their adjacent MEC-elements in

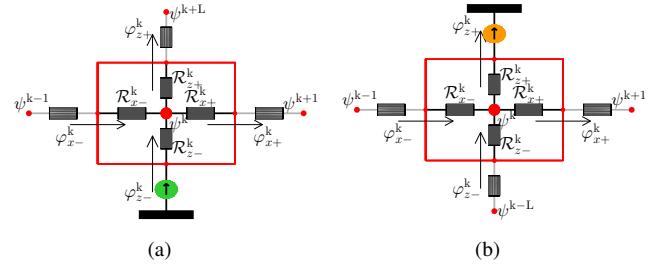


Fig. 8. Illustration of the coupling between the MEC-region and the Fourier region, (a) at the bottom, and (b) at the top.

the  $x$ -direction are replaced according to

$$k-1 = k-1+L \quad \text{for } k = 1 + qL \quad (28)$$

$$k+1 = k+1-L \quad \text{for } k = L + qL \quad (29)$$

where  $q = 0, 1, \dots, K/L - 1$ , and where  $K$  is the total number of MEC-elements in the region. The top and bottom layer of the MEC-region are linked to the Fourier regions that are adjacent at the top or bottom. From the MEC-region, the Fourier regions are considered to be a flux source, therefore, these sources are coupled as shown in Fig. 8. The amplitude of the flux sources is calculated by

$$\varphi_{z-}^k = \iint B_z^{m-1}(x, z)|_{z=h_b} dS_{xy}^k \quad (30)$$

which is the total amount of flux entering through the cross-sectional area at the bottom of a MEC-element in the bottom layer of the MEC-region (region  $m$ ), where  $h_b$  is the  $z$ -coordinate of the boundary between the involved regions (i.e. the MEC-region and the Fourier region underneath). Evaluating the integrations for a unit depth in the  $y$ -direction, the strength of the flux source is given by

$$\begin{aligned} \varphi_{z-}^k = \sum_{n=1}^N \left[ \frac{-1}{\omega_n^{m-1}} (\cos(\omega_n^{m-1} x_1^k) - \cos(\omega_n^{m-1} x_0^k)) B_{zsn}^{m-1}(h_b) \right. \\ \left. + \frac{1}{\omega_n^{m-1}} (\sin(\omega_n^{m-1} x_1^k) - \sin(\omega_n^{m-1} x_0^k)) B_{zcn}^{m-1}(h_b) \right] \quad (31) \end{aligned}$$

where  $B_{zsn}$  and  $B_{zcn}$  are given by (15) and (16), respectively, and  $x_0^k$  and  $x_1^k$  are the left and right  $x$ -coordinate of MEC-element  $k$ , respectively, and  $k$  is bounded by  $1 \leq k \leq L$ , which are all MEC-elements in the bottom layer. Equivalently, the flux at the top of a MEC-element in the top layer of the MEC-region is calculated, with the Fourier description in region  $m+1$  and for MEC-elements  $K - L + 1 \leq k \leq K$ .

## IV. BOUNDARY CONDITIONS

Inside each Fourier and MEC-region, the description of the magnetic field is now defined. To apply the Maxwell's equations throughout the whole domain, these equations should hold on the boundaries between the regions as well. Applying Maxwell's equations to the boundary results in the continuity of both the magnetic flux density normal to the boundary and the magnetic field strength,  $\vec{H}$ , tangential with the boundary,



at the  $z$ -coordinate of this boundary ( $z = h_b$ ). Therefore, the boundary conditions are given by

$$B_z^i(x, z)|_{z=h_b} = B_z^{i+1}(x, z)|_{z=h_b} \quad (32)$$

$$H_x^i(x, z)|_{z=h_b} = H_x^{i+1}(x, z)|_{z=h_b} \quad (33)$$

Using the constitutive relation,  $\vec{B} = \mu_0\mu_r\vec{H} + \mu_0\vec{M}_0$ , with  $\vec{M}_0$  the residual magnetization, (33) becomes

$$\frac{\mu_r^{i+1}}{\mu_r^i} B_x^i(x, h_b) - \frac{\mu_0\mu_r^{i+1}}{\mu_r^i} M_x^i(x) = B_x^{i+1}(x, h_b) - \mu_0 M_x^{i+1}(x). \quad (34)$$

#### A. Boundary conditions between Fourier regions

When both regions  $i$  and  $i+1$  are Fourier regions, the continuity of the normal magnetic flux density and the tangential magnetic field strength is included by means of the separation of variables. Since both regions  $i$  and  $i+1$  have an equal width of the periodicity, their fundamental frequencies are equal. This implies that a separation of the sine and cosine functions is valid, and therefore, for every harmonic  $n$ , equation (32) is given by

$$B_{zsn}^i(h_b) = B_{zsn}^{i+1}(h_b) \quad (35)$$

$$B_{zcn}^i(h_b) = B_{zcn}^{i+1}(h_b) \quad (36)$$

The tangential magnetic field boundary condition (34) for every harmonic  $n$  is given by

$$\frac{\mu_r^{i+1}}{\mu_r^i} B_{xsn}^i(h_b) - \frac{\mu_0\mu_r^{i+1}}{\mu_r^i} M_{xsn}^i = B_{xsn}^{i+1}(h_b) - \mu_0 M_{xsn}^{i+1} \quad (37)$$

$$\frac{\mu_r^{i+1}}{\mu_r^i} B_{xcn}^i(h_b) - \frac{\mu_0\mu_r^{i+1}}{\mu_r^i} M_{xcn}^i = B_{xcn}^{i+1}(h_b) - \mu_0 M_{xcn}^{i+1} \quad (38)$$

With these equations,  $4N$  boundary equations are obtained to solve, together with the other boundary conditions, the  $4N$  unknowns inside a Fourier region (i.e.  $q_n$ ,  $r_n$ ,  $s_n$  and  $t_n$ ).

#### B. Boundary conditions between Fourier and MEC-region

The continuity of the normal magnetic flux density and the tangential magnetic field strength should hold on the boundary between a Fourier region and a MEC-region as well. Since the magnetic flux density in the  $z$ -direction is used as a flux source in the MEC-elements connected to the bottom and top layer of the MEC-region, the continuity of the normal magnetic flux density is already covered.

To ensure the continuity of the tangential magnetic field strength, (34) is rewritten for the MEC-region, given by

$$\frac{\mu_r^k}{\mu_r^{m-1}} B_x^{m-1}(x, h_b) - \frac{\mu_0\mu_r^k}{\mu_r^{m-1}} M_x^{m-1}(x) = B_x^k(x, h_b) - \mu_0 M_x^k(x) \quad (39)$$

where  $k$  is the MEC-element for the observed  $x$ -coordinate, and where  $m-1$  is the Fourier region underneath the MEC-region. The magnetic flux density in the  $x$ -direction for MEC-element  $k$  is found by dividing the average flux in the  $x$ -direction by its cross-sectional area,

$$B_x^k(x, h_b) = \frac{1}{2S_{yz}^k} (\varphi_{x-}^k + \varphi_{x+}^k) \quad (40)$$

where  $\varphi_{x-}$  and  $\varphi_{x+}$  are given in (24) and (25), respectively. Substituting the general expression (11) for the magnetic flux density in the  $x$ -direction for a Fourier region, the tangential magnetic field boundary condition, which should hold for all MEC-elements at the boundary, is given by

$$\sum_{n=1}^N [(B_{xsn}^{m-1}(h_b) - \mu_0 M_{xsn}^{m-1}) \sin(\omega_n^{m-1} x) + (B_{xcn}^{m-1}(h_b) - \mu_0 M_{xcn}^{m-1}) \cos(\omega_n^{m-1} x)] = \frac{\mu_r^{m-1}}{2\mu_r^k S_{yz}^k} \left( \frac{\psi^{k-1} - \psi^k}{\mathcal{R}_{x+}^{k-1} + \mathcal{R}_{x-}^k} + \frac{\psi^k - \psi^{k+1}}{\mathcal{R}_{x+}^k + \mathcal{R}_{x-}^{k+1}} \right) - \frac{\mu_0\mu_r^{m-1}}{\mu_r^k} M_x^k \quad (41)$$

where  $B_{xsn}^{m-1}(h_b)$  and  $B_{xcn}^{m-1}(h_b)$  are given by (13) and (14) with assuming that  $z = h_b$ , the  $z$ -coordinate of the boundary between the MEC-region and the Fourier region below.

Inside the MEC-region, the distribution of the tangential magnetic flux density is a staircase-shaped function, due to the constant magnetic flux density assumed inside the MEC-elements. This staircase-shaped function is described as a Fourier series. Due to the separation of the sine and cosine terms, the tangential magnetic field equations are given by

$$s_n^{m-1} e^{\omega_n^{m-1} h_b} - t_n^{m-1} e^{-\omega_n^{m-1} h_b} - \mu_0 M_{xsn}^{m-1} + \frac{2\mu_r^{m-1}}{x_p \omega_n^{m-1}} \sum_{k=1}^L \left[ \left\{ \frac{1}{2\mu_r^k S_{yz}^k} \left( \frac{\psi^{k-1} - \psi^k}{\mathcal{R}_{x+}^{k-1} + \mathcal{R}_{x-}^k} + \frac{\psi^k - \psi^{k+1}}{\mathcal{R}_{x+}^k + \mathcal{R}_{x-}^{k+1}} \right) - \frac{\mu_0}{\mu_r^k} M_x^k \right\} (\cos(\omega_n^{m-1} x_1^k) - \cos(\omega_n^{m-1} x_0^k)) \right] = 0 \quad (42)$$

$$q_n^{m-1} e^{\omega_n^{m-1} h_b} - r_n^{m-1} e^{-\omega_n^{m-1} h_b} - \mu_0 M_{xcn}^{m-1} - \frac{2\mu_r^{m-1}}{x_p \omega_n^{m-1}} \sum_{k=1}^L \left[ \left\{ \frac{1}{2\mu_r^k S_{yz}^k} \left( \frac{\psi^{k-1} - \psi^k}{\mathcal{R}_{x+}^{k-1} + \mathcal{R}_{x-}^k} + \frac{\psi^k - \psi^{k+1}}{\mathcal{R}_{x+}^k + \mathcal{R}_{x-}^{k+1}} \right) - \frac{\mu_0}{\mu_r^k} M_x^k \right\} (\sin(\omega_n^{m-1} x_1^k) - \sin(\omega_n^{m-1} x_0^k)) \right] = 0 \quad (43)$$

where the summation over all  $L$  elements in the bottom layer of the MEC-region is performed. By taking the average magnetic flux in MEC-element  $k$ , the magnetic scalar potential of three different MEC-elements (i.e. MEC-element  $k$  and its adjacent elements in the  $x$ -direction) is used in each term of the summation. Since the summation is cyclic over the bottom layer (see (28) and (29)) the equations can be rewritten towards

$$s_n^{m-1} e^{\omega_n^{m-1} h_b} - t_n^{m-1} e^{-\omega_n^{m-1} h_b} + \frac{\mu_r^{m-1}}{2S_{yz}} \frac{2}{x_p \omega_n^{m-1}} \sum_{k=1}^L \left[ \frac{1}{\mu_r^{k-1}} \frac{-1}{\mathcal{R}_{x+}^{k-1} + \mathcal{R}_{x-}^k} \cos(\omega_n^{m-1} x) \Big|_{x=x_0^{k-1}}^{x=x_1^{k-1}} + \frac{1}{\mu_r^k} \left( \frac{-1}{\mathcal{R}_{x+}^{k-1} + \mathcal{R}_{x-}^k} + \frac{1}{\mathcal{R}_{x+}^k + \mathcal{R}_{x-}^{k+1}} \right) \cos(\omega_n^{m-1} x) \Big|_{x=x_0^k}^{x=x_1^k} + \frac{1}{\mu_r^{k+1}} \frac{1}{\mathcal{R}_{x+}^k + \mathcal{R}_{x-}^{k+1}} \cos(\omega_n^{m-1} x) \Big|_{x=x_0^{k+1}}^{x=x_1^{k+1}} \right] \psi^k = \mu_0 M_{xsn}^{m-1} + \sum_{k=1}^L \left[ \frac{2\mu_r^{m-1}}{x_p \omega_n^{m-1} \mu_r^k} M_x^k (\cos(\omega_n^{m-1} x_1^k) - \cos(\omega_n^{m-1} x_0^k)) \right] \quad (44)$$

$$q_n^{m-1} e^{\omega_n^{m-1} h_b} - r_n^{m-1} e^{-\omega_n^{m-1} h_b} + \frac{-\mu_r^{m-1}}{2S_{yz}} \frac{2}{x_p \omega_n^{m-1}} \sum_{k=1}^L \left[ \frac{1}{\mu_r^{k-1} \mathcal{R}_{x+}^{k-1} + \mathcal{R}_{x-}^k} \sin(\omega_n^{m-1} x_1^{k-1}) \Big|_{x=x_0^{k-1}} + \frac{1}{\mu_r^k \left( \frac{-1}{\mathcal{R}_{x+}^{k-1} + \mathcal{R}_{x-}^k} + \frac{1}{\mathcal{R}_{x+}^k + \mathcal{R}_{x-}^{k+1}} \right)} \sin(\omega_n^{m-1} x_1^k) \Big|_{x=x_0^k} + \frac{1}{\mu_r^{k+1} \mathcal{R}_{x+}^k + \mathcal{R}_{x-}^{k+1}} \sin(\omega_n^{m-1} x_1^{k+1}) \Big|_{x=x_0^{k+1}} \right] \psi^k = \mu_0 M_{xcn}^{m-1} + \sum_{k=1}^L \left[ \frac{-2\mu_r^{m-1}}{x_p \omega_n^{m-1} \mu_r^k} M_x^k (\sin(\omega_n^{m-1} x_1^k) - \sin(\omega_n^{m-1} x_0^k)) \right]. \quad (45)$$

For the continuity of the tangential magnetic field at the top of the MEC-region, equations (44) and (45) are used for MEC-elements  $K - L + 1 \leq k \leq K$  and for the Fourier quantities of region  $m+1$ .

### C. Non-continuous boundary conditions

Besides the continuous boundaries, other boundary conditions are applicable as well. For a region, which has one of its boundaries at  $z = \pm\infty$ , the magnetic field will vanish towards the boundary. For a Fourier region, this boundary condition is given by

$$B_x^i(x, z) \Big|_{z=\pm\infty} = 0 \quad (46)$$

$$B_z^i(x, z) \Big|_{z=\pm\infty} = 0. \quad (47)$$

Since no sources can exist which have an infinite size, the results from boundary condition derived from  $B_x$  and  $B_z$  become equal. The boundary conditions are, therefore, given by

$$B_{xsn}^i(z) \Big|_{z=\pm\infty} = 0 \quad (48)$$

$$B_{xcn}^i(z) \Big|_{z=\pm\infty} = 0 \quad (49)$$

Substituting (13) and (14), this is simplified to

$$r_n^I = 0 \quad \& \quad t_n^I = 0 \quad \text{if } z = -\infty \quad (50)$$

$$q_n^I = 0 \quad \& \quad s_n^I = 0 \quad \text{if } z = \infty \quad (51)$$

where I depicts the last region of the geometry.

Inside a MEC-region, the same kind of boundary condition can hold if it is assumed that no magnetic field can escape the MEC-region at one of the sides (i.e. the magnetic field is tangential with the boundary). For these situations, the flux in the  $z$ -direction on one of the boundary interfaces is assumed to be zero, therefore, this boundary condition is implemented by assuming that the flux towards this boundary is zero or, equivalently, the reluctance (in the  $z$ -direction) towards this boundary is infinite, given by

$$\text{If } m = 1, \quad \mathcal{R}_{z-}^k = \infty \quad \text{for } 1 \leq k \leq L \quad (52)$$

$$\text{If } m = I, \quad \mathcal{R}_{z+}^k = \infty \quad \text{for } K - L + 1 \leq k \leq K. \quad (53)$$

Finally, the condition that the magnetic field is fully perpendicular to the boundary, is concerned. In fact this boundary condition is equivalent with assuming that the material located on the other side of the boundary has an infinite permeability. This means that the magnetic flux density parallel to

the boundary interface,  $B_x$ , is zero, therefore the following boundary equation is used

$$B_x^i(x, z) \Big|_{z=h_b} = 0 \quad (54)$$

where  $h_b$  is the  $z$ -coordinate of the boundary plane. For a Fourier region, (54) can directly be implemented, by

$$B_{xsn}^i(h_b) = 0 \quad (55)$$

$$B_{xcn}^i(h_b) = 0 \quad (56)$$

For a MEC-region, the boundary condition of (54) is mimicked by assuming that the reluctances in the  $x$ -direction inside the layer of MEC-elements that are the closest to the boundary interface are infinite, as given by

$$\mathcal{R}_{x-}^k = \infty \quad \& \quad \mathcal{R}_{x+}^k = \infty \quad (57)$$

where the boundary elements  $k$  are denoted by

$$1 \leq k \leq L \quad \text{if } m = 1 \quad (58)$$

$$K - L + 1 \leq k \leq K \quad \text{if } m = I. \quad (59)$$

Due to implying an infinite  $x$ -reluctance throughout the full layer of MEC-elements that are closest to the boundary, no magnetic flux in the  $x$ -direction is assumed in this layer of MEC-elements. Therefore, to increase the accuracy of the solution, the size in the  $z$ -direction of the elements adjacent to the boundary should be taken small.

### V. CALCULATING THE COEFFICIENTS

All boundary conditions are known, therefore, the unknown coefficients are solvable. For each Fourier region,  $4N$  a-priori unknown coefficients are used (i.e.  $q_n$ ,  $r_n$ ,  $s_n$  and  $t_n$ ). Furthermore, both at the top and bottom of each Fourier region,  $N$  equations concerning the sine-terms and  $N$  equations concerning the cosine-terms are obtained, independent of the type of boundary conditions used as depicted in Table III. While for the MEC-region, there are  $K$  unknown coefficients (i.e.  $\psi^k$ ), for which  $K$  independent equations are given (based on Kirchhoff's current law (23)).

To solve all unknowns, the boundary conditions and coefficients are collected in one matrix equation, given by

$$\underbrace{\begin{bmatrix} E_b^1 \\ E_t^1 \\ E_b^2 \\ \vdots \\ E_b^{m-1} \\ E_{MEC}^{m-1} \\ E_{KCL} \\ E_{MEC}^{m+1} \\ E_t^{m+1} \\ E_b^{m+2} \\ \vdots \\ E_t^I \end{bmatrix}}_{E_{tot}} \underbrace{\begin{bmatrix} Q^1 \\ Q^2 \\ \vdots \\ Q^{m-1} \\ \Psi \\ Q^{m+1} \\ Q^{m+2} \\ \vdots \\ Q^I \end{bmatrix}}_X = \underbrace{\begin{bmatrix} Y_b^1 \\ Y_t^1 \\ Y_b^2 \\ \vdots \\ Y_b^{m-1} \\ Y_{MEC}^{m-1} \\ Y_{KCL} \\ Y_{MEC}^{m+1} \\ Y_t^{m+1} \\ Y_b^{m+2} \\ \vdots \\ Y_t^I \end{bmatrix}}_{Y_{tot}} \quad (60)$$

where  $E$  are the sine and cosine equations of the boundary conditions of the Fourier region (according to Table III)



TABLE III  
EQUATIONS USED FOR BOUNDARY CONDITIONS OF A FOURIER REGION

Type	Continuous Top	Continuous Bottom	MEC	Zero-flux	$\mu = \infty$
Sine	(35)	(37)	(44)	(48)	(55)
Cosine	(36)	(38)	(45)	(49)	(56)

with trailing and/or leading zeros to ensure the connection to the correct coefficients,  $\mathbf{Y}$  are the terms in the boundary conditions that are not dependent on the unknown coefficients (i.e. the source terms),  $\mathbf{Q} = [\mathbf{q}_n, \mathbf{r}_n, \mathbf{s}_n, \mathbf{r}_n]^T$  represents the column vector with Fourier unknowns, and  $\mathbf{\Psi}$  is a column vector with the magnetic potential inside all MEC-elements. Furthermore, the subscripts  $b$  and  $t$  represent the bottom and top of the region, while  $\mathbf{E}_{MEC}$  is given by (44) and (45), and  $\mathbf{E}_{kcl}$  is given by (23), and where I indicates the last region considered.

Before solving this set of matrix equations, the coefficients that are directly found by a boundary condition (i.e. (50) and (51)) should be removed from the set of equations, together with the corresponding boundary conditions. Afterwards, the matrix equation (60) is solved using an LU-decomposition, and all the (a-priori) unknown coefficients are found.

## VI. FORCE CALCULATION

With all coefficients defined, the magnetic flux density throughout the whole domain is known, therefore, for calculation of the force on a part of the geometry, the Maxwell stress tensor is applied. By defining the integration domain as a closed box around the part of the domain for which the force desired (including air), an accurate calculation of the force is obtained with a numerical integration. As derived in [26], the force density per unit depth on a 2-D geometry is given by

$$F_x = \frac{1}{\mu_r \mu_0} \left\{ - \int_{C_b} B_x B_z dx - \int_{C_l} \left( \frac{1}{2} B_x^2 - \frac{1}{2} B_z^2 \right) dz + \int_{C_t} B_x B_z dx + \int_{C_r} \left( \frac{1}{2} B_x^2 - \frac{1}{2} B_z^2 \right) dz \right\} \quad (61)$$

$$F_z = \frac{1}{\mu_r \mu_0} \left\{ - \int_{C_b} \left( \frac{1}{2} B_z^2 - \frac{1}{2} B_x^2 \right) dx - \int_{C_l} B_z B_x dz + \int_{C_t} \left( \frac{1}{2} B_z^2 - \frac{1}{2} B_x^2 \right) dx + \int_{C_r} B_z B_x dz \right\} \quad (62)$$

where  $C_b$ ,  $C_l$ ,  $C_t$  and  $C_r$  are the bottom, left, top and right edges of the integration domain, respectively.

## VII. MODEL VALIDATION

The proposed hybrid analytical modeling (HAM) method is validated using 2-D Finite Element Analysis (FEA) models for the shielding and multi-tooth motor geometry given in Fig. 1 and 2, respectively. The 2-D FEA models are implemented in

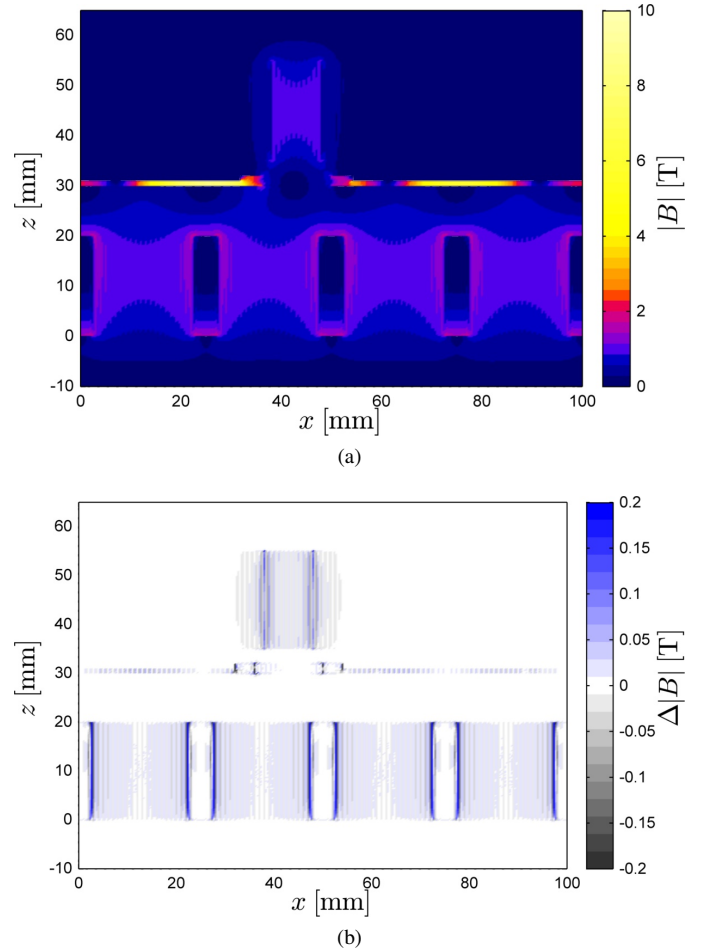


Fig. 9. The magnetic flux density for the shielding geometry of Fig. 1, with (a) the absolute value obtained with the proposed HAM, and (b) the difference between FEA and HAM,  $\Delta|B| = |B_{FEA}| - |B_{HAM}|$ .  $N = 100$  harmonics are used in all Fourier regions and an  $x \times z$ -discretization of  $265 \times 22$  is used in Region 4.

FLUX2D [27] and are densely meshed, while the periodicity, and all material properties and geometrical parameters are equal to the implemented hybrid analytical models.

For the shielding geometry shown in Fig. 1, the magnitude of the magnetic flux density obtained with the hybrid analytical modeling is shown in Fig. 9(a). As it is visible, a smooth magnetic flux density pattern is obtained with the proposed hybrid method. In Fig. 9(b), the difference between the FEA results and the HAM results is shown as,  $\Delta|B| = |B_{FEA}| - |B_{HAM}|$ . In the regions where the permanent magnets are located, the harmonic description of the permanent magnets is clearly visible (i.e. the Gibbs phenomenon [28]). For the permanent magnet of the voice coil, a deviation is visible that is extending further in the  $x$ -direction than inside the magnet array. Furthermore, some deviations are shown inside the MEC-region. These deviations are mainly due to the discretization of the MEC-region, where the magnetic flux density contains discrete steps instead of the desired smooth pattern.

A more thorough comparison between the results obtained, with finite element analysis and the hybrid analytical model, for the shielding geometry is given in Fig. 10, where the magnetic flux density on a path in the middle of the shield

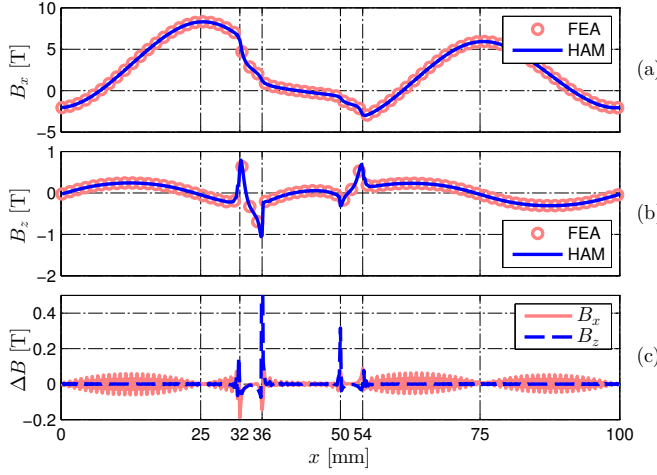


Fig. 10. The magnetic flux density in the middle of the shield ( $z = 30.5$  [mm]) for the FEA and HAM. (a) the magnetic flux density in the  $x$ -direction, (b) the magnetic flux density in the  $z$ -direction, and (c) the difference between FEA and HAM,  $\Delta|B| = |B_{FEA}| - |B_{HAM}|$ .

( $z = 30.5$  [mm]) is shown. Observing  $B_x$  and  $B_z$ , the HAM closely matches the FEA results. However, the differences, shown in Fig. 10(c), clearly reveal the deviations. For the magnetic flux density in the  $x$ -direction a discretization noise is visible, the amplitude of the noise increases with the derivative of  $B_x$ . Furthermore, for both  $B_x$  and  $B_z$ , there are deviations visible around the edges of the shield (at  $x = 36$  [mm] and  $x = 50$  [mm]). The remaining large differences are located around the edges of the thickening of the shield.

For a numerical comparison, the force per unit depth in the  $x$ - and  $z$ -direction on the permanent magnet of the voice coil actuator obtained from FEA and HAM is given in Table IV. Besides the calculated force, the difference in force between the FEA and HAM are given as well, where  $\Delta F_x < 1$  [%] and  $\Delta F_z \approx 3$  [%].

For the multi-tooth motor geometry shown in Fig. 2, the absolute value of the magnetic flux density obtained with HAM is shown in Fig. 11(a). Again a rather smooth magnetic flux density pattern is obtained with the proposed hybrid method. In Fig. 11(b), the difference between the FEA results and the HAM results is shown,  $\Delta|B| = |B_{FEA}| - |B_{HAM}|$ . Besides the edges of the high permeable material, only small deviations are visible.

A more thorough comparison between the finite element and hybrid analytical results for the multi-tooth motor is given in Fig. 12, where the magnetic flux density in the center of the airgap ( $z = 17.75$  [mm]) is shown. The HAM is visually similar with the FEA results when observing the  $B_x$  and  $B_z$ . The difference between the FEA and HAM, shown in Fig. 12(c), clearly shows a deviation between the models. Most of these deviations, for both  $B_x$  and  $B_z$ , occur around the edges of the teeth of either the stator or the mover. Note that it is well known that an accurate prediction of the magnetic flux density obtained with FEA is not ensured around the edges of a material.

For a numerical comparison, the force per unit depth on the mover in the  $x$ - and  $z$ -direction calculated from FEA and

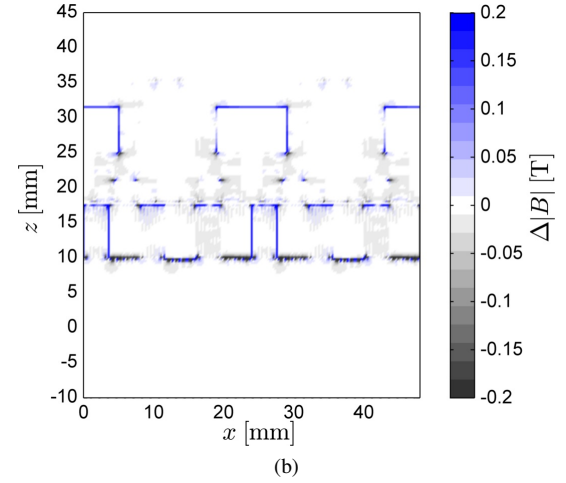
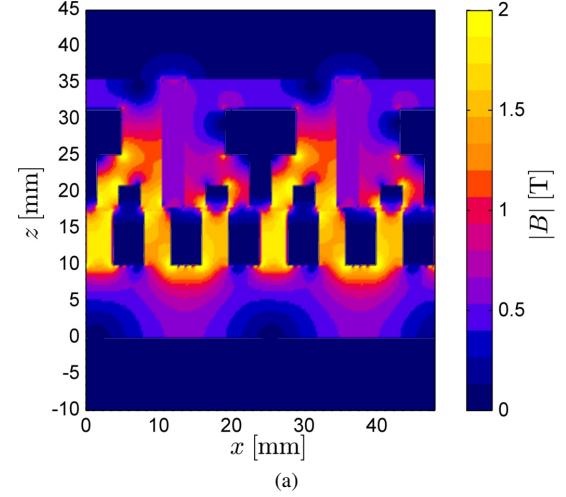


Fig. 11. The magnetic flux density for the multi-tooth motor geometry of Fig. 2, with (a) the absolute value obtained with the proposed HAM, and (b) the difference between FEA and HAM,  $\Delta|B| = |B_{FEA}| - |B_{HAM}|$ .  $N = 100$  harmonics are used in all Fourier regions, and an  $x \times z$ -discretization of  $127 \times 33$  and  $225 \times 73$  is used in Regions 3 and 5, respectively.

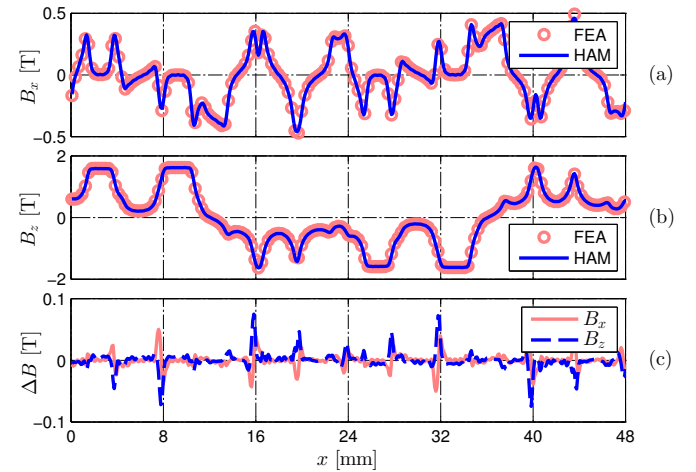


Fig. 12. The magnetic flux density in the middle of the airgap ( $z = 17.75$  [mm]) of Fig. 2 for FEA and HAM. (a) The magnetic flux density in the  $x$ -direction, (b) the magnetic flux density in the  $z$ -direction, and (c) the difference between (FEA) and HAM,  $\Delta|B| = |B_{FEA}| - |B_{HAM}|$ .

TABLE IV

THE FORCE ON THE PERMANENT MAGNET OF THE VOICE-COIL ACTUATOR AND THE MOVER OF THE MULTI-TOOTH MOTOR.

	Voice-coil		Multi-tooth motor	
	$F_x$ [N/m]	$F_z$ [N/m]	$F_x$ [N/m]	$F_z$ [N/m]
FEA	121.6	327.5	238	$-15.9 \cdot 10^3$
HAM	121.6	317.7	235	$-16.0 \cdot 10^3$
$\Delta F$ [N/m]	-0.05	9.83	3.02	141
$\Delta F$ [%]	-0.05	3.09	2.24	-0.89

TABLE V

THE SIMULATION PARAMETERS FOR THE VOICE-COIL ACTUATOR AND THE MULTI-TOOTH MOTOR FOR HAM.  $N$  IS THE NUMBER OF HARMONICS AND "TIME" IS THE SIMULATION TIME INCLUDING MESHING, SOLVING AND CALCULATING  $B$ -FIELD AND FORCE.

	Voice-coil HAM	Multi-tooth motor HAM
$N$	100	100
mesh-size	$265 \times 22$	$97 \times 33$ $169 \times 73$
Time [min]	1.25	12

HAM is given in Table IV. Besides of the calculated force, the difference in force between the FEA and HAM are given as well, where  $\Delta F_x < 1.5$  [%] and  $\Delta F_z < 1$  [%].

In Table V, the simulation parameters for the HAM are given. For the MEC-regions, the number of mesh elements is included by "number of mesh-elements in  $x \times$  number of mesh-elements in  $z$ ". The simulation time includes meshing, solving and calculation of the  $B$ -field and force.

## VIII. DISCUSSION

In the previous section, it has been shown that the magnetic flux density distribution found with the proposed Hybrid 2-D model with respect to 2-D FEA gives accurate results. In the proposed HAM method, the benefits of two analytical modeling methods are combined, i.e. Fourier modeling and mesh-based MEC modeling. Both analytical modeling methods have some drawbacks which have been highlighted in the results of the previous section.

The differences in the predicted magnetic flux density inside the regions with a permanent magnet clearly reveals the harmonic description (i.e. Gibbs phenomenon). The deviations occurring are due to the description of a rectangular shaped magnetization function with a number of harmonics. A more noticeable difference is visible in Region 6 when compared to Region 2 of Fig. 9(b). The deviations between the models extends further in the  $x$ -direction in Region 6 due to the assumption of a full region with one single permeability. In the HAM, the full region has the permeability of the permanent magnet, while the FEA only uses this permeability inside the permanent magnet itself.

Since the HAM method uses a mesh-based MEC-approach, the mesh density is an important factor in the HAM. As especially visible in Fig. 10(c), the meshing of the MEC-region results in a discretization error. The discretization noise is caused by the fact that the coordinates, on which the magnetic flux density is extracted from the HAM, are not the points

on which the magnetic scalar potential is calculated during solving. The mesh-based MEC modeling assumes an equal magnetic flux density inside each of the flux tubes illustrated in Fig. 6, therefore the most accurate result is obtained in the potential node. Between two potential nodes, the magnetic flux density is assumed constant, which results in a "staircase"-shaped flux density. To reduce this discretization error, the number of MEC-elements inside the MEC-region could be increased.

Another deviation caused by the discretization is visible around the edges of the materials, clearly shown in Fig. 11(b). On the edges of the materials, the magnetic permeability will change rapidly. Due to the calculation of the magnetic flux according to equations (24) to (27), the changing permeability will be visible between the two potential nodes located around the material edge. By decreasing the size of the MEC-elements around the edges of the materials, the deviation of the magnetic flux density around these edges is decreased.

Only linear materials are assumed in the shown formulation, which results in the very large magnetic flux density occurring inside the magnetic shield of Fig. 9(a). These magnetic flux density values will most definitely cause saturation inside the magnetic shield. Saturation effects are not included in the modeling, however, based on an iterative process the magnetic permeability of the materials inside the MEC-layer can be changed. Therefore, local saturation effects can be included in the MEC-region of the HAM, while only global saturation effects can be included in most other analytical modeling methods.

As previously indicated, the accuracy of the magnetic flux density results increases when the number of harmonics taken into account is increased. However, due to the large difference in values in the  $E$ -matrix (60), which are caused by the positive and negative exponential values in the Fourier modeling, singularity in the matrix might occur. This singularity limits the number of harmonics since the harmonic number  $n$  is used in the exponential terms.

An increase in the number of MEC-elements gives a more accurate solution, however, increasing the mesh-density, in equality with FEA, will result in a larger computational effort. From computational point of view, the proposed HAM is less computational intensive with respect to FEA, especially since only a part of the domain is meshed. A large, additional reduction of the computational efforts is possible in the HAM, since the current implementation is not optimized for calculation time. For both the FEA and the HAM, a trade-off should be made between the desired mesh-density and the resulting calculation times. However, since the HAM only meshes the regions with changing material properties, the airgap of a motor is not meshed, while especially in the airgap of a machine, a high mesh-density in FEA is required for an accurate result.

A significant reduction in calculation time of the magnetic field and force is possible for certain variations. Since all source terms (i.e. the magnetization and current density terms) are collected in the  $Y_{tot}$ -matrix, variations of the source amplitude and movement the source in the  $x$ -direction is included by only recalculating  $Y_{tot}$ . A movement of a source

in the  $z$ -direction or movement of (and movement within) the MEC-region requires recalculation of the full system of linear equations.

The proposed modeling method is not only suited for geometries in cartesian coordinate systems. With the adaption of the harmonic description according to [9], polar and cylindrical coordinate systems are possible as well.

## IX. CONCLUSION

The principle of combining Fourier modeling with mesh-based Magnetic Equivalent Circuit (MEC) modeling is demonstrated on two electromagnetic examples. It is shown that the Hybrid Analytical Modeling (HAM) technique can be applied to any geometry where a periodicity is present or can be assumed in cartesian coordinate systems. With the inclusion of the mesh-based MEC modeling, the possibilities and applicability of the modeling for geometries with small features of high-permeable material, such as saliency, tooth-shoes and slot shapes, is increased. Since HAM describes the airgap region of a machine by means of a Fourier series, it requires a less dense meshing compared to finite element analysis.

For the electromagnetic example structures shown in this paper, an excellent agreement is obtained with respect to finite element analysis, which proves the applicability of this modeling method for a wide class of electromagnetic devices. For the forces calculated with the hybrid analytical model, less than 3 [%] deviation with respect to finite element analysis is obtained.

## REFERENCES

- [1] J. L. Coulomb, "A methodology for the determination of global electromechanical quantities from a finite element analysis and its application to the evaluation of magnetic forces, torques and stiffness," *Magnetics, IEEE Transactions on*, vol. 19, no. 6, pp. 2514–2519, 1983.
- [2] H. C. Roters, *Electromagnetic Devices*. New York: Wiley, 1941.
- [3] V. Ostovic, *Dynamics of Saturated Electric Machines*. New York: Springer-Verlag, 1989.
- [4] E. P. Furlani, *Permanent Magnet and Electromechanical Devices*, I. Mayergoyz, Ed. Elsevier, 2001.
- [5] J. L. G. Janssen, B. L. J. Gysen, J. J. H. Paulides, and E. A. Lomonova, "Advanced electromagnetic modeling applied to anti-vibration systems for high precision and automotive applications," *International Com-pumag Society Newsletter*, vol. 1, no. 19, pp. 3–16, Jan 2012.
- [6] G. Akoun and J. P. Yonnet, "3D analytical calculation of the forces exerted between two cuboidal magnets," *Magnetics, IEEE Transactions on*, vol. 20, no. 5, pp. 1962–1964, 1984.
- [7] M. F. J. Kremers, J. J. H. Paulides, E. Ilhan, J. L. G. Janssen, and E. A. Lomonova, "Relative permeability in a 3D analytical surface charge model of permanent magnets," *Magnetics, IEEE Transactions on*, vol. 49, no. 5, pp. 2299–2302, 2013.
- [8] B. Hague, *The Principles of Electromagnetism, Applied to Electrical Machines*, 1st ed. New York: Dover Publications, Inc., 1962, formerly titled: *Electromagnetic Problems in Electrical Engineering*.
- [9] B. L. J. Gysen, K. J. Meessen, J. J. H. Paulides, and E. A. Lomonova, "General formulation of the electromagnetic field distribution in machines and devices using fourier analysis," *Magnetics, IEEE Transactions on*, vol. 46, no. 1, pp. 39–52, Jan 2010.
- [10] J. Caldwell, "Modifications of the fourier approach for magnetic field calculations to include axial shields in superconducting magnets," *Journal of Applied Physics*, vol. 56, no. 11, pp. 3338–3340, 1984.
- [11] K. J. W. Pluk, J. W. Jansen, and E. A. Lomonova, "Magnetic shielding for coreless linear permanent magnet motors," *Applied Mechanics and Materials*, vol. 416, pp. 45–52, 2013.
- [12] M. F. J. Kremers, E. Ilhan, D. C. J. Krop, J. J. H. Paulides, and E. A. Lomonova, "Reluctance network model for the in-wheel motor of a series-hybrid truck using tooth contour method," in *Electromagnetic Field Computation (CEFC), 2010 14th Biennial IEEE Conference on*, 2010.
- [13] E. Ilhan, M. F. J. Kremers, E. T. Motoasca, J. J. H. Paulides, and E. A. Lomonova, "Spatial discretization methods for air gap permeance calculations in double salient traction motors," *Industry Applications, IEEE Transactions on*, vol. 48, no. 6, pp. 2165–2172, 2012.
- [14] G. Xiong and S. A. Nasar, "Analysis of fields and forces in a permanent magnet linear synchronous machine based on the concept of magnetic charge," *Magnetics, IEEE Transactions on*, vol. 25, no. 3, pp. 2713–2719, 1989.
- [15] J. M. M. Rovers, J. W. Jansen, and E. A. Lomonova, "Modeling of relative permeability of permanent magnet material using magnetic surface charges," *Magnetics, IEEE Transactions on*, vol. 49, no. 6, pp. 2913–2919, 2013.
- [16] D. T. E. H. v. Casteren, J. J. H. Paulides, and E. A. Lomonova, "3-D numerical surface charge model including relative permeability : the general theory," *Magnetics, IEEE Transactions on*, vol. 50, no. 11, Accepted for publication, 2014.
- [17] K. J. W. Pluk, G. De Gersem, J. W. Jansen, and E. A. Lomonova, "Fourier modeling of magnetic shields with linear permeable material and finite dimensions," *Magnetics, IEEE Transactions on*, vol. 49, no. 7, pp. 4160–4163, 2013.
- [18] M. Amrhein and P. T. Krein, "3-D magnetic equivalent circuit framework for modeling electromechanical devices," *Energy Conversion, IEEE Transactions on*, vol. 24, no. 2, pp. 397–405, June 2009.
- [19] C. B. Rasmussen and E. Ritchie, "A magnetic equivalent circuit approach for predicting pm motor performance," in *Industry Applications Conference, 1997. Thirty-Second IAS Annual Meeting, IAS '97., Conference Record of the 1997 IEEE*, vol. 1, Oct 1997, pp. 10–17 vol.1.
- [20] J. Perho, *Reluctance Network for Analysing Induction Machines*, ser. Acta polytechnica Scandinavica: El. Finnish Acad. of Technology, 2002.
- [21] S. Ouagued, Y. Amara, and G. Barakat, "Comparison of hybrid analytical modelling and reluctance network modelling for pre-design purposes," in *Proceedings of ELECTRIMACS 2014*, 2014, pp. 238–243.
- [22] G. Barakat and Y. Amara, "A simple and effective way to couple analytical formal solution of magnetic potential and reluctance network models," in *Computation in Electromagnetics (CEM 2014), 9th IET International Conference on*, March 2014.
- [23] Y. Laoubi, M. Dhifli, G. Verez, Y. Amara, and G. Barakat, "Open circuit performance analysis of a permanent magnet linear machine using a new hybrid analytical model," *Magnetics, IEEE Transactions on*, Accepted for publication.
- [24] M. Mirzayee, H. Mehrjerdi, and I. Tsurkerman, "Analysis of a high-speed solid rotor induction motor using coupled analytical method and reluctance networks," in *Wireless Communications and Applied Computational Electromagnetics, 2005. IEEE/ACES International Conference on*, April 2005, pp. 537–540.
- [25] J. Cai, Q. Lu, Y. Jin, C. Chen, and Y. Ye, "Performance investigation of multi-tooth flux-switching pm linear motor," in *Electrical Machines and Systems (ICEMS), 2011 International Conference on*, Aug 2011, pp. 1–6.
- [26] K. J. W. Pluk, J. W. Jansen, and E. A. Lomonova, "Force measurements on a shielded coreless linear permanent magnet motor," *Magnetics, IEEE Transactions on*, vol. 50, no. 11, pp. 1–4, Nov 2014.
- [27] Cedrat, *FLUX 11.1.0, User's guide*, Meylan, France, 2012.
- [28] J. W. Gibbs, "Fourier series," *Nature* 59, 200 and 606., 1899.